ACS APPLIED MATERIALS & INTERFACES

Research Article

Cite This: ACS Appl. Mater. Interfaces XXXX, XXX, XXX−XXX

www.acsami.org

# Top Illuminated Hysteresis-Free Perovskite Solar Cells Incorporating Microcavity Structures on Metal Electrodes: A Combined Experimental and Theoretical Approach

Chintam Hanmandlu,[†,‡] Chi-Ching Liu,[†] Chien-Yu Chen,[§] Karunakara Moorthy Boopathi,[†] Shang-Hsuan Wu,[†] Mriganka Singh,[†] Anisha Mohapatra,[†] Hao-Wu Lin,[*,§] Yia-Chung Chang,[†] Yun-Chorng Chang,[†] Chao-Sung Lai,[*,‡,⊥,#] and Chih-Wei Chu[*,†,§,∥]

[†]Research Center for Applied Science, Academia Sinica 128, Academia Road, Section 2, Nangang Taipei 11529 Taiwan (R.O.C.)

[‡]Department of Electronic Engineering, Chang Gung University, Wenhua first Road, Guishan District, Taoyuan City 33302, Taiwan (R.O.C.)

[§]Department of Materials Science and Engineering, National Tsing Hua University, No. 101, Section 2, Kuang-Fu Road, Hsinchu 30013, Taiwan (R.O.C.)

[∥]College of Engineering, Chang Gung University, No. 259, Wenhua first Road, Guishan District, Taoyuan City 33302, Taiwan (R.O.C.)

[⊥]Department of Nephrology, Chang Gung Memorial Hospital, Linkou, New Taipei City 33305, Taiwan (R.O.C.)

[#]Department of Materials Engineering, Ming Chi University of Technology, 84 Gungjuan Road, Taishan, New Taipei City, 24301, Taiwan (R.O.C)

Supporting Information

**ABSTRACT:** Further technological development of perovskite solar cells (PSCs) will require improvements in power conversion efficiency and stability, while maintaining low material costs and simple fabrication. In this Research Article, we describe top-illuminated ITO-free, stable PSCs featuring microcavity structures, wherein metal layers on both sides on the active layers exerted light interference effects in the active layer, potentially increasing the light path length inside the active layer. The optical constants (refractive index and extinction coefficient) of each layer in the PSC devices were measured, while the optical field intensity distribution was simulated using the transfer matrix method. The photocurrent densities of perovskite layers of various thicknesses were also simulated; these results mimic our experimental values exceptionally well. To modify the cavity electrode surface, we deposited a few nanometers of ultrathin $MoO_3$ (2, 4, and 6 nm) in between the Ag and poly(3,4-ethylenedioxythiophene):polystyrenesulfonate (PEDOT:PSS) layers provide hydrophobicity to the Ag surface and elevate the work function of Ag to match that of the hole transport layer. We achieved a power conversion efficiency (PCE) of 13.54% without hysteresis in the device containing a 4 nm-thick layer of $MoO_3$. In addition, we fabricated these devices on various cavity electrodes (Al, Ag, Au, Cu); those prepared using Cu and Au anodes displayed improved device stability of up to 72 days. Furthermore, we prepared flexible PSCs having a PCE of 12.81% after incorporating the microcavity structures onto poly(ethylene terephthalate) as the substrate. These flexible solar cells displayed excellent stability against bending deformation, maintaining greater than 94% stability after 1000 bending cycles and greater than 85% after 2500 bending cycles performed with a bending radius of 5 mm.

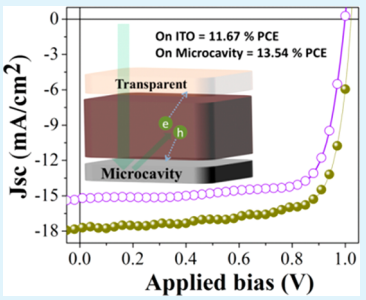


**KEYWORDS:** *microcavity structures, ITO-free, perovskite solar cells, top illumination, stability*

## 1. INTRODUCTION

Thin film photovoltaics incorporating inorganic/organic hybrid perovskite materials are promising candidates for future low-cost, high-performance, clean energy devices because of their low material and processing costs, ambipolar behavior, high diffusion length, and direct bandgap.[1−5] Perovskite solar cells (PSCs) have two types of device structures: mesoporous and planar heterojunction. The best mesoporous PSC-based on the n−i−p structure has displayed a power conversion efficiency (PCE) of 22.1% when incorporating high-temperature-sintered mesoporous $TiO_2$ as the electron transport layer (ETL).[6] Unfortunately, this high-temperature ETL increases the cost of the fabrication process and is not conducive to the development of flexible PSCs. Solution-processable organic layers are alternatives that have been exploited as charge extraction layers in planar PSCs having a p−i−n structure on flexible substrates.[7]

Received: March 16, 2018
Accepted: May 8, 2018
Published: May 8, 2018





DOI: 10.1021/acsami.8b04329
ACS Appl. Mater. Interfaces XXXX, XXX, XXX−XXX

Notably, PSCs with p−i−n structures have fascinated researchers because of their hysteresis-less behavior and low-temperature fabrication.[8] Recently, a PCE of 20% was reported for a PSC having a p−i−n structure almost equal to that of a PSC having a n−i−p structure.[9]

Taking advantage of low-temperature fabrication processes, PSCs having a p−i−n structure have been reported on polymers and rigid substrates when using indium tin oxide (ITO) as an anode.[7−9] Transparent conductive oxides (TCOs) usually have relatively low sheet resistivity, high conductivity, and excellent transmission properties in the visible range of wavelengths; accordingly, they have been used as standard anodes in the fabrication of thin film solar cells.[8,9] Nevertheless, the use of TCOs has its drawbacks, including fragility against bending on polymer substrates, low conductivity compared with the metal electrode, and high prices because indium is less-earth-abundant material; these characteristics affect their roll-to-roll fabrication on polymer substrates.[7,10−12] As replacements for TCOs, other functional materials [e.g., graphene, carbon nanotubes, PEDOT:PSS] have been tested for the fabrication of thin film solar cells.[13−18] These materials have excellent transmission properties at visible wavelengths, but their conductivities are lower than those of the metal electrodes. Moreover, the PCE of PSCs incorporating these electrodes are relatively low, due to its underling contacting with the other layers (e.g., charge extraction and perovskite layers).[19,20] In particular, we have previously reported the incorporation of TCO-free top-illuminated microcavity structures into organic solar cells, thereby increasing the light path length inside the active layer.[21] These microcavity devices have more complicated structures when compared with conventional ITO cells, with the photoactive layer sandwiched between two metallic electrodes: an ultrathin metal film working as the front electrode and an opaque metal film as the back electrode. These microcavity structures have several advantages when used in thin film solar cells: they can confine incident light with resonant frequencies in between the two metal electrodes because of optical coherent interference; they increase the light path length in thin film solar cells; and they maintain efficient charge dissociation and extraction.[22,23] Moreover, these ultrathin metal electrodes can be prepared readily through thermal vapor deposition; the electrode exhibits very low sheet resistivity; good transmission occurs for visible wavelengths; and the ultrathin metal electrodes can be prepared on various substrates.[21,24−26] Furthermore, thin metal electrodes have good bending stability, so they can be used in flexible solar cells and continuous roll-to-roll fabrication. In this regard, thermally deposited thin metal layers appear to be the best choice when preparing TCO-free efficient PSCs.

In this study, we developed semitransparent metal electrodes [(Cu (1 nm)/Ag (10 nm)] exhibiting a combination of good optical transparency and electrical conductivity. We studied the electro-optics within the microcavity structured PSCs both theoretically and experimentally. On the basis of our simulations, the optical field intensity distributions within the microcavity structured PSCs were significantly influenced by the active layer when various wavelengths of light illuminated the electrode. The higher wavelengths of light leaving the active layer increased the light path length inside the active layer because of optical interference with the cavity electrode. These theoretical simulations were in good agreement with the experimental results. Depositing ultrathin $MoO_3$ layers (only a few nanometers in thickness) between the back electrode and PEDOT:PSS enhanced the work function (WF) and decreased the hydrophobicity of the back electrode (Ag). After optimizing the thickness of the ultrathin $MoO_3$ layer on Ag, we achieved a PCE of 13.54% with negligible current density−voltage ($J$−$V$) hysteresis when incorporating the microcavity structured electrodes. We investigated the effect of ultrathin $MoO_3$ on Ag by analyzing the hydrophobicity of the back electrode surfaces, the electrode WFs, the surface morphologies of the films, and the optical and device properties. In addition, we tested the fabrication of these PSC devices on various (Al, Cu, Ag, Au) microcavity structures; those incorporating Au and Cu exhibited improved device stability up to 72 days when operated in a $N_2$-filled glovebox, providing results comparable to those of a semitransparent PSC device having an ITO electrode. Furthermore, we prepared flexible PSCs featuring the microcavity structures on a PET substrate, obtaining a PCE of 12.81%. These flexible devices also displayed excellent stability against bending deformation, maintaining greater than 94% of the original efficiency after 1000 bending cycles and greater than 85% after 2500 bending cycles, when applying a bending radius of 5 mm.

## 2. EXPERIMENTAL SECTION

**2.1. Methylammonium Iodide (MAI).** HI (57 wt % in water), methylamine ($CH_3NH_2$, 40 wt % in water), $PbI_2$ (99.998%), dimethyl sulfoxide (DMSO), and diethyl ether were purchased from Alfa Aesar and used without purification. MAI ($CH_3NH_3I$) was synthesized by reacting aqueous HI (15 mL) with $CH_3NH_2$ (13.5 mL) at 0 °C for 2 h in three-neck flask under a $N_2$ atmosphere with constant stirring. A white precipitate ($CH_3NH_3I$) formed during rotary evaporation of the solvent. The precipitated white powder was collected, washed three times with diethyl ether, and then dried under vacuum at 60 °C overnight. This dried powder was stored in a glovebox.

**2.2. Solar Cell Device Fabrication and Characterization.** The solar cell devices were fabricated on opaque Ag electrodes (deposited through thermal evaporator), having a thickness of 120 nm, on various substrates. Ultrathin $MoO_3$ layers having thicknesses from 2 to 6 nm were deposited on the Ag, with various substrates, at a deposition rate of 0.1 to 0.5 Å/s using a thermal evaporator, followed by annealing at 150 °C for 10 min. The deposition rate and thicknesses were monitored during deposition using a quartz crystal sensor. A uniform layer of PEDOT:PSS was spin-coated (4000 rpm, 60 s) onto the $MoO_3$ surface, followed by annealing (130 °C, 30 min). The substrates with PEDOT:PSS were transferred to a glovebox for deposition of the perovskite active layer using a thermal annealing interdiffusion method. KCl was added to the $PbI_2$ precursor to give a uniform perovskite crystalline structure.[27] Perovskite layers of various thicknesses were prepared from $PbI_2$ (130−400 mg/mL) and KCl (3−7.5 mg) dissolved in DMSO (1 mL); MAI was dissolved in 2-propanol (15−40 mg/mL). Both solutions were kept on a hot plate at 70 °C overnight. A hot $PbI_2$/salt mixture with DMSO as solvent was spin-coated (4500 rpm, 40 s) on PEDOT:PSS and annealed directly at 70 °C for 30 min. The MAI solution was spin-coated (4500 rpm, 40 s) onto the $PbI_2$ film and then annealed at 105 °C for 65 min to form a crystalline perovskite film. A solution (20 mg/mL) of [6,6]-phenyl-$C_{61}$-butyric acid methyl ester (PCBM) in chlorobenzene was spin-coated (6000 rpm, 40 s) onto the perovskite layer, followed by annealing (100 °C, 40 min). The device was completed through thermal evaporation of $C_{60}$ (20 nm). Films of BCP (8 nm) and Cu (1 nm)/Ag (10 nm) were deposited through a shadow mask. Finally, films of capping layer ($MoO_3$) (20, 40, and 60 nm) were deposited under vacuum ($1 \times 10^{-6}$ mbar). The active area of each device having a flexible or rigid substrate was 0.1 $cm^2$.

A home-built panchromatic optical field simulation program, coded in MATLAB and based on the transfer matrix method, was used to model the optical field distributions and exciton formation. Transmission spectra of the transparent electrode thin films were measured


DOI: 10.1021/acsami.8b04329
ACS Appl. Mater. Interfaces XXXX, XXX, XXX−XXX

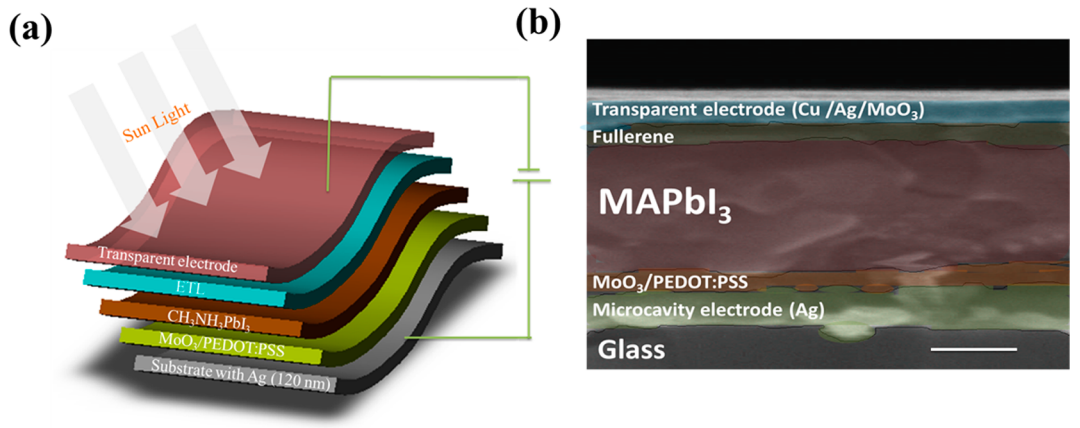


**Figure 1.** (a) Schematic representation of a top-illuminated PSC having a microcavity structure. (b) Cross-sectional SEM image of a representative PSC (scale bar = 500 nm).

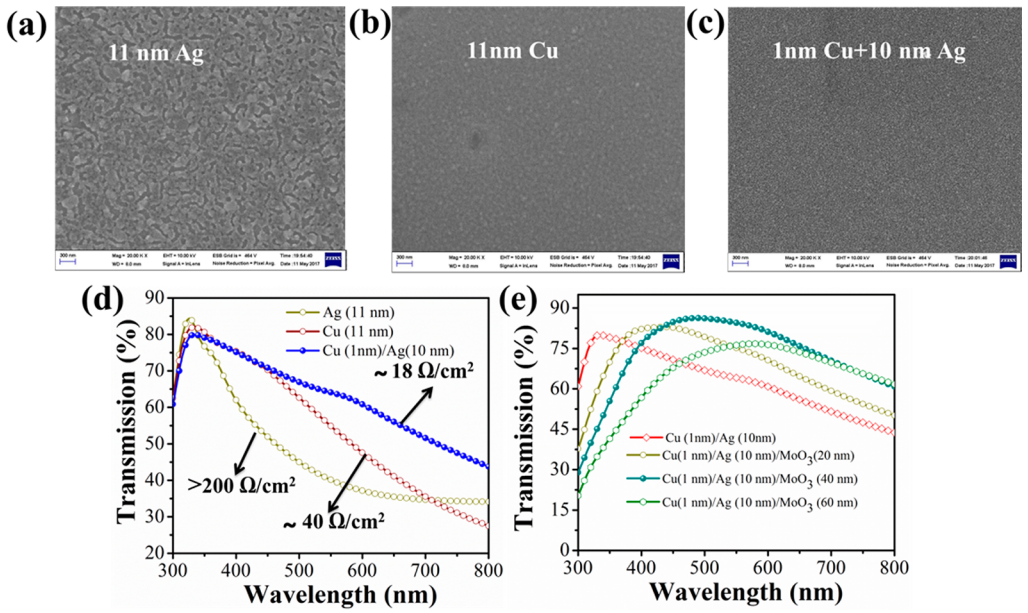


**Figure 2.** (a–c) Morphologies of 11 nm pristine silver (Ag) and copper (Cu) films: (a) Ag, (b) Cu, and (c) Cu-seeded Ag. (d) UV–vis transmission and conductivity of Cu, Ag, and Cu-seeded Ag. (e) UV–Vis transmission of Cu-seeded Ag electrodes with capping layers of various thicknesses.

using a Jacob V-670 UV–vis spectrometer. Refractive indices and extinction coefficients were measured using a variable-angle spectroscopic ellipsometer (J. A. Woollam V-VASE). All measurements were made at room temperature. EQE spectra were obtained under short-circuit conditions. The devices were encapsulated before they were removed from the glovebox for EQE measurement. The light source was a 75-W Xe lamp (Enlitech, QE-R3011); the light output from the monochromator was focused on the photovoltaic cell being tested in DC mode operation. The devices were illuminated inside a glovebox by a Xe lamp as a solar simulator (Thermal Oriel 1000 W), which provided a simulated AM 1.5 spectrum (100 mW $cm^{-2}$). The light intensity was calibrated using a monosilicon photodiode with a KG-5 color filter (Hamamatsu). Atomic force microscopy (ASYLUM, MFP-3D) was used to measure the surface topography and roughness. Fluorescence lifetime decays were obtained under excitation at 485 nm and 5 MHz; the signal was focused on a PDM single photon avalanche diode (SPAD) from MPD and then processed through PicoHarp 300 Time-Correlated Single Photon Counting (TCSPC) data acquisition.

## 3. RESULTS AND DISCUSSION

**3.1. Device Architecture, Transparent Electrode, and Perovskite Morphology on Cavity Electrode.** The fabrication of the PSC devices and the processing conditions are presented in the Experimental Section. Figure 1a and b presents a schematic representation and a cross-sectional scanning electron microscopy (SEM) image, respectively, of a top-illuminated PSC presenting Cu/Ag/$MoO_3$ as the top transparent electrode. The device was fabricated on thermally deposited Ag/glass or a PET pattern (active area = 2 mm × 5 mm). On top of the cavity electrode we deposited $MoO_3$ layers that were a few nanometers thick (2, 4, or 6 nm) through thermal vapor deposition, followed by thermal annealing at 150 °C on a hot plate. By varying the thickness of the $MoO_3$ layer from 0 to 6 nm, the WF increased from 4.27 to 5.10 eV and the hydrophobicity of the cavity electrode decreased. We prepared planar p–i–n PSCs using PEDOT:PSS and fullerenes as the hole (HTL) and electron (ETL) transport layers, respectively. Finally, the devices were completed through sequential thermal evaporation of the hole blocking layer (BCP), Cu, Ag, and the capping layer ($MoO_3$), thereby forming the multilayer transparent electrode.


DOI: 10.1021/acsami.8b04329
ACS Appl. Mater. Interfaces XXXX, XXX, XXX–XXX

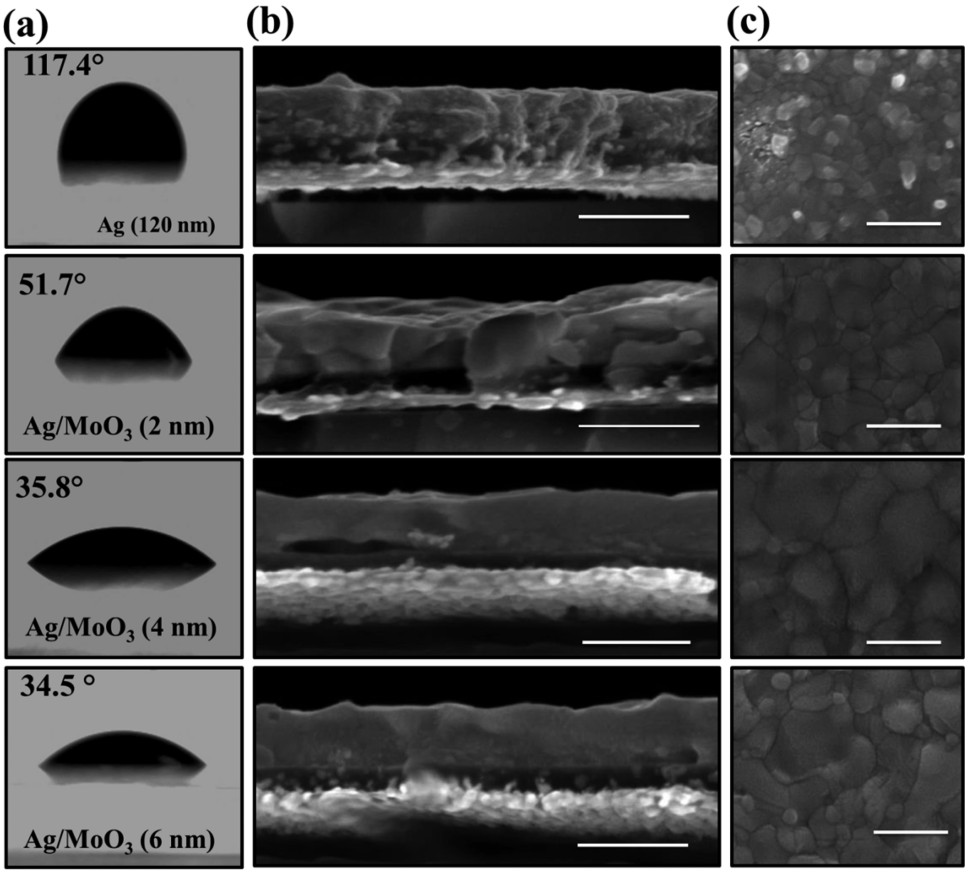


**Figure 3.** (a) Contact angles of PEDOT:PSS on $MoO_3$ films of various thicknesses on metal electrode. (b) Cross-sectional and (c) top-view SEM images of 280 nm perovskite grown on Ag electrodes presenting doped $MoO_3$ of various thicknesses. Scale bars in panels b and c: 500 nm.

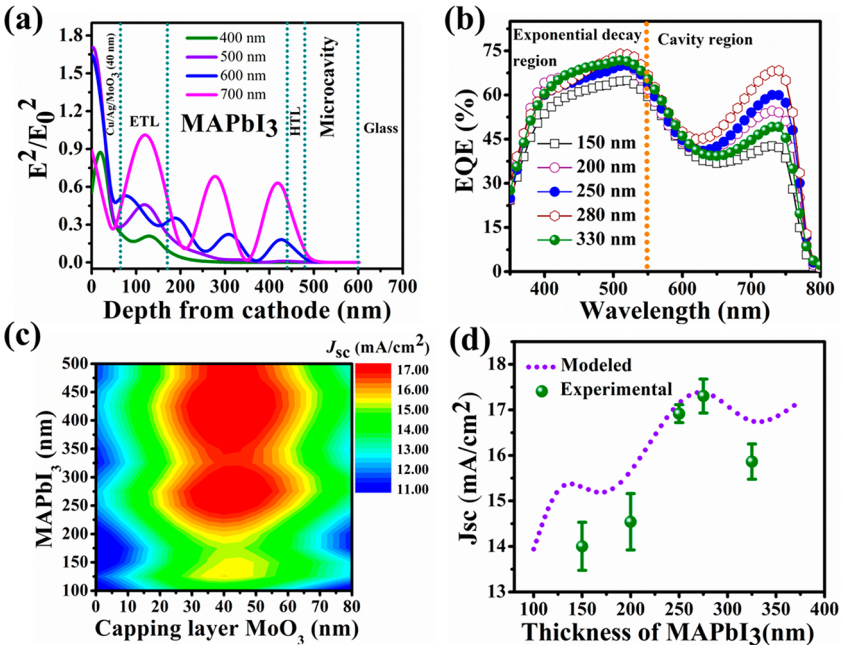


**Figure 4.** (a) Optical field distributions in PSCs at four wavelengths: for $\lambda \leq 500$ nm, the plot follows exponential decay in the active layers; for $\lambda > 500$, the optical field distribution is governed by cavity interference. (b) EQE spectra of PSC devices with active layers of various thicknesses. (c) Simulated values of $J_{sc}$ plotted with respect to the thicknesses of the active layer and capping layer. (d) Experimental and modeled values of $J_{sc}$ plotted with respect to the active layer thickness.

Two characteristics are most important for the transparent electrodes of PSCs solar cells: sufficiently high conductivity for charge collection from the extraction layer, and high transmission for visible and near-infrared wavelengths. Neat 11 nm-



DOI: 10.1021/acsami.8b04329
ACS Appl. Mater. Interfaces XXXX, XXX, XXX−XXX

thick Ag and Cu films formed discontinuous islands through volmore growth during thermal vapor deposition, with resistivities greater than 200 and 40 Ω/□, respectively (Figure 2a and b). Because Cu has a higher surface energy than Ag,[28] we introduced 1 nm of Cu as a seeded layer to enhance the wettability of Ag. As a result, the Ag atoms attached well to the Cu surface, leading to Frank van der Merwe growth and the formation of a continuous ultrathin Ag film (Figure 2c). The resistivity of the film decreased to approximately 18 Ω/□ and the transmission of the electrode was superior to those of the 11 nm Ag and Cu films for visible wavelengths (Figure 2d). To increase the transmission of the electrode for visible and near-infrared wavelengths, we deposited a capping layer of $MoO_3$, which has a high refractive index and low extinction coefficient (Figure S1i), on this electrode. Figure 2e displays the different thicknesses of the capping layers deposited on the ultrathin hybrid metal; upon varying the thickness from 20 to 60 nm, we found that a 40 nm-thick capping layer provided good transmission in the visible and near-infrared regions.

The wettability of PEDOT:PSS on nonwetting Ag surfaces is challenging when fabricating high-quality perovskite thin films; we used contact angle measurements to investigate this behavior in the presence and absence of the ultrathin $MoO_3$ layers. Figure 3a displays optical microscopy images of PEDOT:PSS deposited on Ag surfaces in the presence and absence of the $MoO_3$ layer. In the absence of the $MoO_3$ layer, the contact angle of PEDOT:PSS was 117.4° ± 0.6° (i.e., its surface was hydrophobic); $MoO_3$ thicknesses of 2, 4, and 6 nm on the Ag surface decreased the contact angle to 51.7° ± 0.25°, 35.8° ± 0.05°, and 34.5° ± 0.1°, respectively (Figure 3a). The perovskite film was fabricated on the PEDOT:PSS layer through thermal annealing-induced interdiffusion method.[29,30] Cross-sectional and top-view SEM images of perovskite films on the PEDOT:PSS layers in the presence and absence of the $MoO_3$ layers on Ag (Figure 3b and c) reveal a clear correlation between the substrate surface wetting and the film morphology. In the presence of $MoO_3$, the perovskite film morphology on PEDOT:PSS was more uniform and had larger grains than was the case in the absence of the $MoO_3$ film, where the morphology was not uniform and pinholes existed between the grains (Figure 3c). The uniform perovskite film formed good interfacial contact with the charge extraction layers, potentially allowing efficient charge extraction and minimizing recombination losses.[9]

**3.2. Experimental and Theoretical Approach.** We used transfer matrix method analysis to understand the electro-optics of top-illuminated PSCs through cavity modeling and simulated the optical field distributions in the devices.[31,32,21] The refractive index (and extinction coefficient) of each layer in the PSC devices applied in the transfer matrix model was analyzed through ellipsometry (Figure S1). Figure 4a presents a simulation of the optimized device structure glass/Ag (120 nm)/$MoO_3$(4 nm)/PEDOT:PSS (40 nm)/$MAPbI_3$ (280 nm)/PCBM (85 nm)/$C_{60}$ (20 nm)/BCP (8 nm)/Cu (1 nm)/Ag (10 nm)/$MoO_3$ (40 nm) for four incident wavelengths. The optical field intensity distribution depended strongly on the position of the PSCs and the wavelength of the incident light. For wavelengths of less than 500 nm, the optical field intensity distribution was governed by the Beer–Lambert law, with an exponential dependence of the optical field intensity distribution in the PSCs, because of the high extinction coefficient of perovskite layers at a wavelength of 500 nm (Figure S1a). For wavelengths of greater than 500 nm, however, the optical field intensity distribution in a low-finesse thin film optical interference regime was similar to our previous observations in organic solar cells.[21] These observations suggested that the external quantum efficiencies (EQEs) of perovskite active layers of various thicknesses were fully saturated for wavelengths of less than 500 nm, but for wavelengths greater than 500 nm the EQEs strongly depended on the active layer thickness.

The calculations suggested that, for optimization, we should focus on achieving maximum photon harvesting for wavelengths greater than 500 nm, where the EQE strongly depended on the thickness of the perovskite active layer. This phenomenon was confirmed in the experimental data in Figure 4b, which plots the experimental EQEs of active layers of various thicknesses. For wavelengths of less than 500 nm, the dependence of the EQE on the active layer was minimal, but for wavelengths greater than 500 nm the EQE was fully dependent on the thickness of the active layer because of the effect of optical interference with the cavity electrode. The thickness of the ETL and HTL layers was another important consideration because it could impact the values of $J_{sc}$ (Figure S2). For a 280 nm-thick active layer, increasing the thickness of the PCBM layer resulted in the absorption of more light, thereby decreasing the value of $J_{sc}$; in contrast, the thickness of the PEDOT:PSS layer had an insignificant effect on the value of $J_{sc}$ (Figure S2). Hence, we predicted that thinner ETLs and HTLs would provide superior device performance. Figure 4c plots the simulated values of $J_{sc}$ with respect to the thicknesses of the perovskite and capping layers. An active layer thickness of greater than 280 nm provided a good quality perovskite film, but the experimental values of $J_{sc}$ were relatively low because of charge recombination in the active layer (Figure S3).[24] For a constant-thickness capping layer (40 nm), varying the thickness of the active layer provided experimental values of $J_{sc}$ that matched the simulated values exceptionally well (Figure 4d). Hereafter, for optimal charge carrier transport, we used a 280 nm-thick perovskite active layer for device fabrication on both glass and flexible substrates.

**3.3. Photovoltaic Performance of PSCs with Various Doped $MoO_3$ Thicknesses on Cavity Electrode.** To investigate the effect of the thickness of the ultrathin films of doped $MoO_3$ on the device performance, we tested $MoO_3$ layers of four different thicknesses (0, 2, 4, and 6 nm) on the bottom Ag cavity electrode. Table 1 summarizes the resultant photovoltaic properties of the best devices with two directions; from reverse voltage, to forward voltage denoted R-F, and in the backward scan direction, from forward bias to reverse bias

**Table 1. Photovoltaic Parameters of Devices Incorporating Ultrathin $MoO_3$ of Various Thicknesses Doped on the Cavity Electrode Ag**

| $MoO_3$ thickness on Ag (nm) | scan direction | $J_{sc}$ (mA/cm$^2$) | PCE (%) | $V_{oc}$ (V) | FF (%) | hysteresis index |
|---|---|---|---|---|---|---|
| 0 | F | 10.11 | 3.41 | 0.80 | 42.16 | 0.52 |
| | R | 10.51 | 4.83 | 0.88 | 52.22 | |
| 2 | F | 15.32 | 9.43 | 0.98 | 62.80 | 0.04 |
| | R | 15.56 | 9.59 | 0.95 | 64.87 | |
| 4 | F | 17.80 | 13.46 | 1.02 | 73.80 | 0.001 |
| | R | 17.88 | 13.54 | 1.03 | 73.85 | |
| 6 | F | 17.28 | 12.18 | 1.00 | 70.60 | 0.008 |
| | R | 17.35 | 12.25 | 1.00 | 70.48 | |


DOI: 10.1021/acsami.8b04329
ACS Appl. Mater. Interfaces XXXX, XXX, XXX–XXX

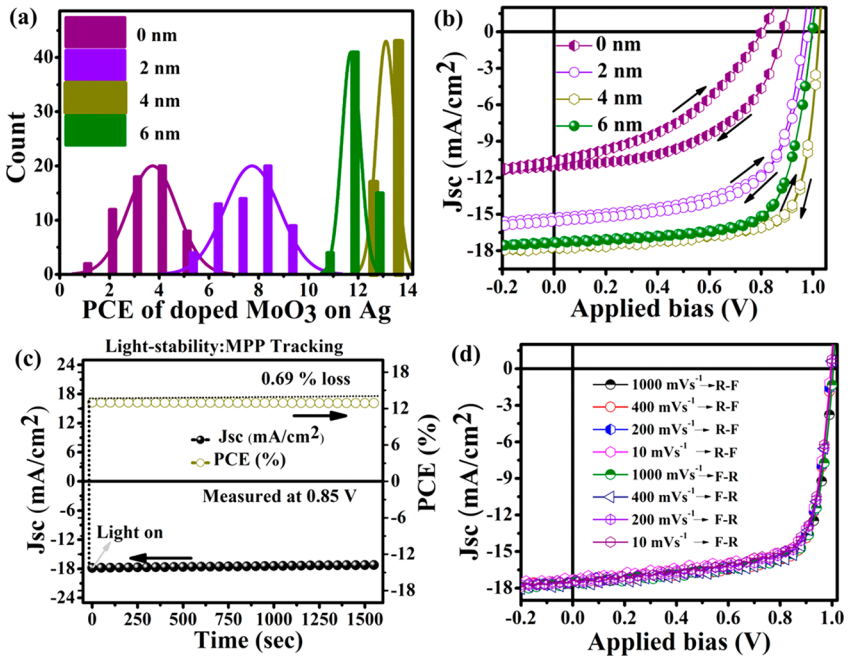


**Figure 5.** (a) Efficiency histogram of 60 devices with various thicknesses of doped $MoO_3$ on Ag. (b) $J-V$ characteristics of best performing devices having various thicknesses of doped $MoO_3$ on Ag, measured with forward and reverse biases. (c) $J-V$ characteristics of PSC devices measured through forward and reverse scans with different dwelling times, at 10 mV per step. (d) PCE of the device doped with 4 nm $MoO_3$ on Ag, held for 25 min at the maximum power point under illumination of 1 sun.

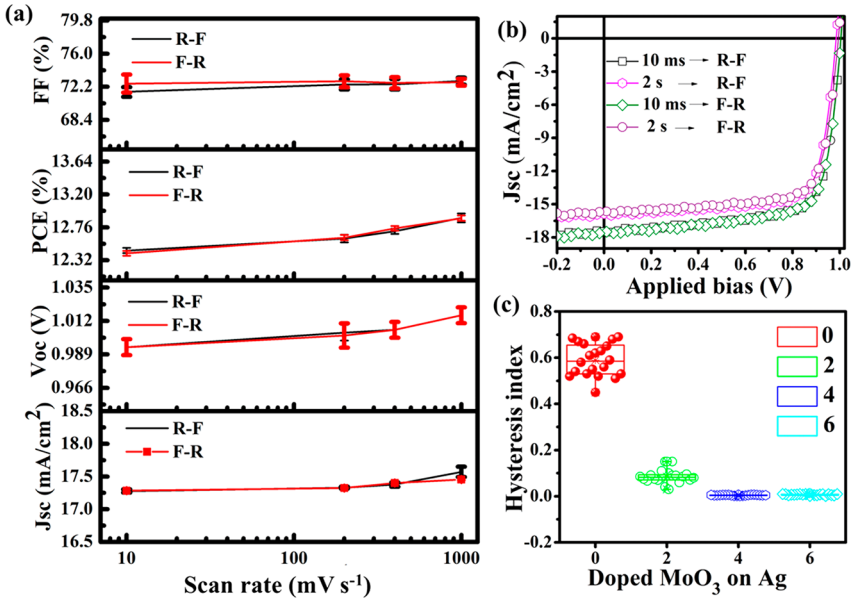


**Figure 6.** (a) Photovoltaic parameters of PSC devices measured through forward and reverse scans with different scan rates, at 10 mV per step. (b) $J-V$ characteristics of PSC devices measured through forward and reverse scans with different dwelling times (10 ms and 2 s) at 10 mV per step. (c) Dependence of the hysteresis index on various thicknesses of $MoO_3$-doped on cavity electrode.

denoted F-R. Figure 5a presents the average PCEs of 60 $MoO_3$-containing devices, and Figure S4 provides the corresponding fill factors (FFs) and vales of $V_{oc}$ and $J_{sc}$. For convenience, the electrodes doped with the ultrathin $MoO_3$ layers are named Ag-M0, Ag-M2, Ag-M4, and Ag-M6, where the number refers to the thickness (nm) of the $MoO_3$ layer. The PCEs of Ag-M0 varied widely because the PEDOT:PSS film and the perovskite solution were not wetted with the hydrophobic Ag surface. In case of Ag-M2, the PCEs also varied widely, from 5 to 9.59%, presumably because of the nonuniform coating of PEDOT:PSS on the Ag-M2 surface. The 2 nm ultrathin $MoO_3$ failed to cover the hydrophobic Ag surface thoroughly; therefore, the resulting $J-V$ characteristics were inconsistent, and we observed photocurrent hysteresis among the devices (Figure 5b). The devices with slightly thicker $MoO_3$ layers exhibited slightly less variation in performance, with the PCEs of the devices based on Ag-M4 and Ag-M6 increasing to 13.54 and 12.25%, respectively. Figure 5b displays the $J-V$ curves of the best performing devices containing each of the thicknesses of the doped ultrathin $MoO_3$ on Ag. Among them, the highest PCE


DOI: 10.1021/acsami.8b04329
ACS Appl. Mater. Interfaces XXXX, XXX, XXX−XXX

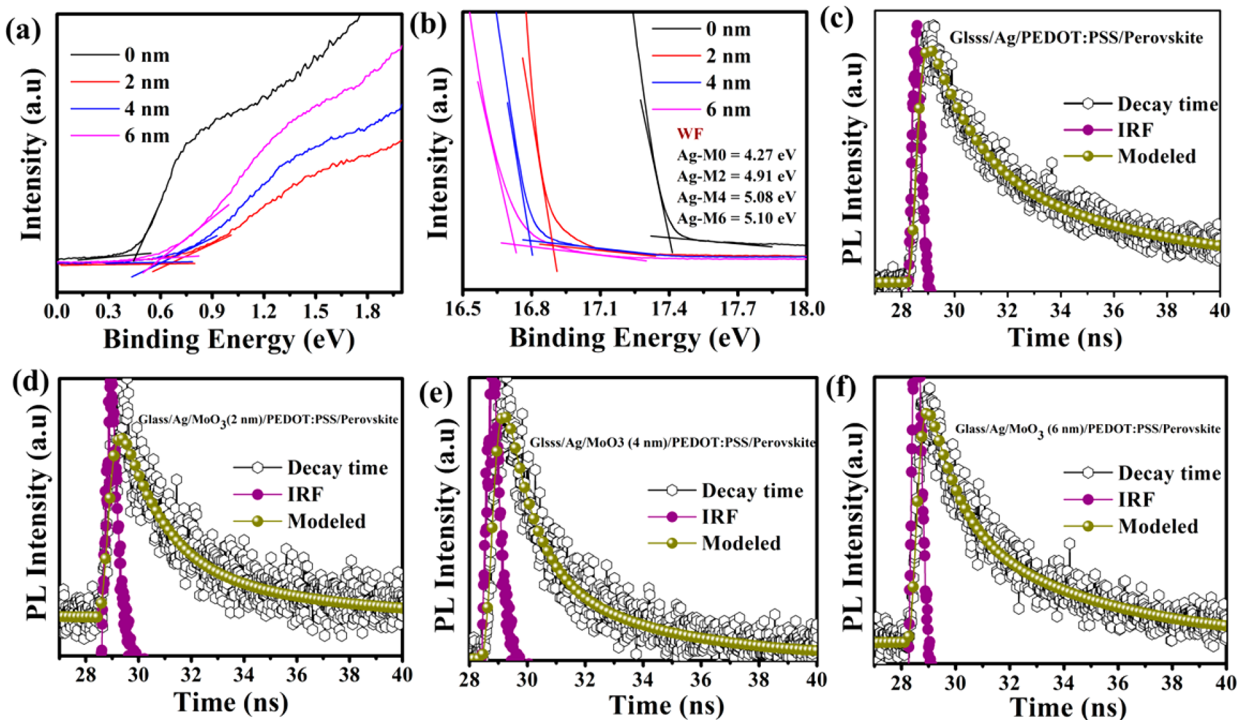


**Figure 7.** (a) UPS photoemission cutoff and (b) valence band spectra. (c–f) Transient PL decay curves of devices incorporating (c) perovskite A-M0, (d) A-M2, (e) A-M4, and (f) A-M6.

was 13.54%; to the best of our knowledge, this efficiency is highest ever reported for top-illuminated PSCs with TCO-free metal electrodes (Table S1). Each of these layer thicknesses not only increased the device performance but also exhibited hysteresis-free characteristics with negligible differences between the R-F and F-R scan directions. To perform the stability analysis of the best cell, we recorded the steady state photo current output for 1550 s, at a bias of 0.85 V, which corresponds to the maximum power point (Figure 5c). The PCE remained almost constant within this length of time, confirming the stability of the PSC cells on the metal electrodes.

**3.4. Hysteresis.** The origin of hysteresis in PSCs exists due to trapping and detrapping of charge carriers, ferroelectricity, thickness changes in absorbing layer or contact conductivity with electron and hole transport materials and ion migration.[33−35] All of these parameters are related to the perfect formation of a perovskite layer film. The absence of hysteresis in our devices, it displays that our fabrication procedure were presented here is excellent to control the hysteresis behavior in $J-V$ cures of the cavity structure based devices. To investigate the hysteresis behavior of our microcavity structure based device with Ag-M4, we measure their $J-V$ parameters at different scan rates from 10, 200, 400, and 1000 $mVs^{-1}$ in R-F (−1.0 to 1.2 V) and F-R (1.2 to −1.0 V) scan directions and compared in Figure 5d and Figure 6a. The difference in $V_{oc}$ reduced for F-R and R-F directions is about ∼20 mV slightly decreased when scan rate reduced from 1000 to 10 $mVs^{-1}$, while the difference in $J_{sc}$, FF, and PCE slightly decreased. Figure 6b displays the $J-V$ parameters of PSCs devices with different dwelling times 10 ms and 2 s (1000 and 5 $mVs^{-1}$) between the intervals. When an interval time increased to 2 s of dwelling time, resulted in a higher FF and $J_{sc}$ and $V_{oc}$ is less in both directions which leads to decrease the PCE of device (Figure S5).[36] To get more information regarding of this hysteresis behavior in $J-V$ characteristics, we calculated the hysteresis index (HI) using the equation

$$\mathrm{HI} = \frac{J_{RS}(0.8V_{oc}) - J_{FS}(0.8V_{oc})}{J_{RS}(0.8V_{oc})} \quad (1)$$

where $J_{RS}$ $(0.8V_{oc})$ and $J_{FS}$ $(0.8V_{oc})$ represents the $J_{sc}$ at 80% of $V_{oc}$ for R-F and F-R scan directions, respectively. Figure 6c summarizes the statistical analysis of HI extracted from the $J-V$ curves of 20 independent devices. The HI values are high in case of Ag-M0 and Ag-M2 compared with Ag-M4 and Ag-M6; the reduction of $MoO_3$ thicknesses on cavity electrode, resulted significant increase in HI values from 0.001 to 0.52 (Table S1). With 0 and 2 nm thicknesses of $MoO_3$ on cavity electrode, it forms insufficient gap states on the electrode because the insufficient of holes are collected to the cavity electrode.[37−39] The variation of $J_{sc}$ relatively insignificant in Ag-M4 and Ag-M6 and the HI values of these two types of devices difference is less.

**3.5. Thin-Film Characterizations.** We used ultraviolet photoemission spectroscopy (UPS) to determine the effect of the thickness of the ultrathin $MoO_3$ layers on the WF of the Ag electrode. Figure 7a and b presents the direct photoemissions of the Ag electrodes covered with the ultrathin $MoO_3$ layers (0, 2, 4, and 6 nm). Figure 7a displays the top of the occupied states or position of the valence band maximum (VBM); Figure 7b reveals the photoemission cut-offs from which the WFs of the surfaces were extracted. From the above two energies, the WFs of the Ag electrodes in the presence and absence of the ultrathin $MoO_3$ layers were calculated using the equation

$$\mathrm{WF} = 21.2\ \mathrm{eV} - (E_{cutoff} - \mathrm{VBM})\ \mathrm{eV} \quad (2)$$

Figure S8 presents the full UPS spectra of the various ultrathin $MoO_3$ presenting Ag electrodes. As displayed in Figure 7 the deposition of the 2 nm-thick $MoO_3$ layer shifted


DOI: 10.1021/acsami.8b04329
ACS Appl. Mater. Interfaces XXXX, XXX, XXX−XXX

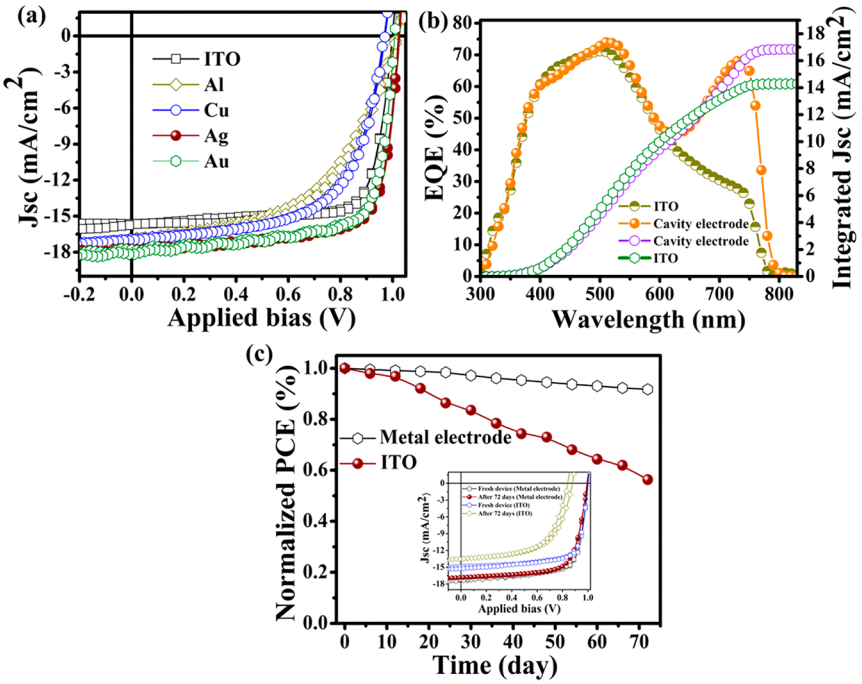


**Figure 8.** (a) $J-V$ characteristics of PSC devices featuring various microcavity-structure electrodes and ITO. (b) EQE spectra and integrated values of $J_{sc}$ of devices incorporating ITO and cavity electrodes. (c) Normalized PCE and $J-V$ curves (inset) of devices having the cavity and ITO electrodes, after storage in a $N_2$-filled glovebox.

the photoemission cutoff to higher energy, thereby increasing the WF from 4.27 to 4.91 eV. Thicker $MoO_3$ layers of 4 and 6 nm increased the WF slightly, to 5.08 and 5.10 eV, respectively. Effective hole collection from the active layer requires a decrease in the energy barrier between the anode and the HTL. As revealed in Table 1, the higher value of $J_{sc}$ and the higher PCE of Ag-M4 mainly resulted from the increased WF of Ag, thereby increasing the hole collection to the electrode. The PCE of the device decreased upon increasing the thickness of the ultrathin $MoO_3$ layer to 6 nm. Thermally evaporated $MoO_3$ has a very deep valence band edge; accordingly, holes can be transported through gap states in the $MoO_3$ layer formed near the metal contact.[37,38] If we increase the thickness of the ultrathin $MoO_3$ layer, the lack of gap states would not facilitate quasi ohmic contact for efficient hole extraction;[38,39] for this reason, the value of $J_{sc}$ and the PCE of the Ag-M6 device both decreased.

The value of $V_{oc}$ also can depend on the quality of the interface between the layers. We used atomic force microscopy (AFM) to study the surface morphologies of the cavity electrode after deposition of various thicknesses of $MoO_3$ and the PEDOT:PSS films. The root-mean-square (rms) roughness of the samples Ag-M0, Ag-M2, Ag-M4, and Ag-M6 were 4, 1.74, 1.4, and 1.3 nm, respectively (Figure S7). The roughness of Ag-M4 was less than those of Ag-M0 and Ag-M2. A better interface can be created between the layers when the underlying layers are less rough; for this reason, we observed an increase in the value of $V_{oc}$ of the device.[40]

Time-resolved photoluminescence spectroscopy (TRPL) revealed the charge transfer kinetics from the perovskite absorbers to PEDOT:PSS in the presence of the Ag-M0-, Ag-M2-, Ag-M4-, Ag-M6-modified electrodes. Figures 7c–f and S8 display the TRPL spectra of perovskite films in the presence and absence of the extraction layer on Ag. We modeled the PL decay time and amplitudes using the biexponential equation

$$f(t) = \sum_i \mathrm{Ai}\exp\left(\frac{-t}{\tau i}\right) + B \tag{3}$$

where $A_i$ is the decay amplitude, $\tau_1$ is the slow decay time component, $\tau_2$ is the fast decay component, and $B$ is the constant for baseline offset. Table S2 lists the parameters obtained from such analysis for all conditions. For the glass/Ag/perovskite sample, the PL decay life times $\tau_1$ and $\tau_2$ were 9.29 and 60.76 ns, respectively, with corresponding amplitudes of 37.66% and 20.97%, respectively. In case of the glass/Ag/PEDOT:PSS/perovskite sample, these PL decay life times were 10.18 and 1.73 ns, respectively, with corresponding amplitudes of 24.98 and 37.99%, respectively. When ultrathin $MoO_3$ (2 and 4 nm) layers introduced between the Ag and PEDOT:PSS films, the values of both $\tau_1$ and $\tau_2$ decreased [5.86/1.49 ns (2 nm); 3.9/0.85 ns (4 nm)] and the corresponding amplitudes were 26.19/33.15% (2 nm) and 6.62/14.19% (4 nm). Furthermore, when 6 nm $MoO_3$ was present, to the values of $\tau_1$ and $\tau_2$ increased to 5.5 and 1.03 ns, respectively, with corresponding amplitudes of 25.39% and 19.87%, respectively. In cases of Ag/$MoO_3$ (2, 6 nm)/PEDOT:PSS/perovskite, the fast and slow decay life times were higher, suggesting that depopulation of photogenerated charges was dominated by charge collection to the Ag/$MoO_3$/PEPDOT:PSS/perovskite interface and appropriated recombination loss. In the case of Ag/$MoO_3$ (4 nm)/PEDOT:PSS/perovskite, the fast and slow decay lifetimes of the charges were lower, suggesting that the majority of charge carriers collected at the electrode occurred with less recombination loss. The high charge transfer and efficient charge collection exhibited in the device having the structure Ag/$MoO_3$ (4 nm)/PEDOT:PSS/perovskite were presumably closely related to the lower interfacial barrier and more efficient charge carrier extraction to the electrode, thereby contributing to the enhanced photovoltaic properties and FF of this device.


DOI: 10.1021/acsami.8b04329
ACS Appl. Mater. Interfaces XXXX, XXX, XXX–XXX

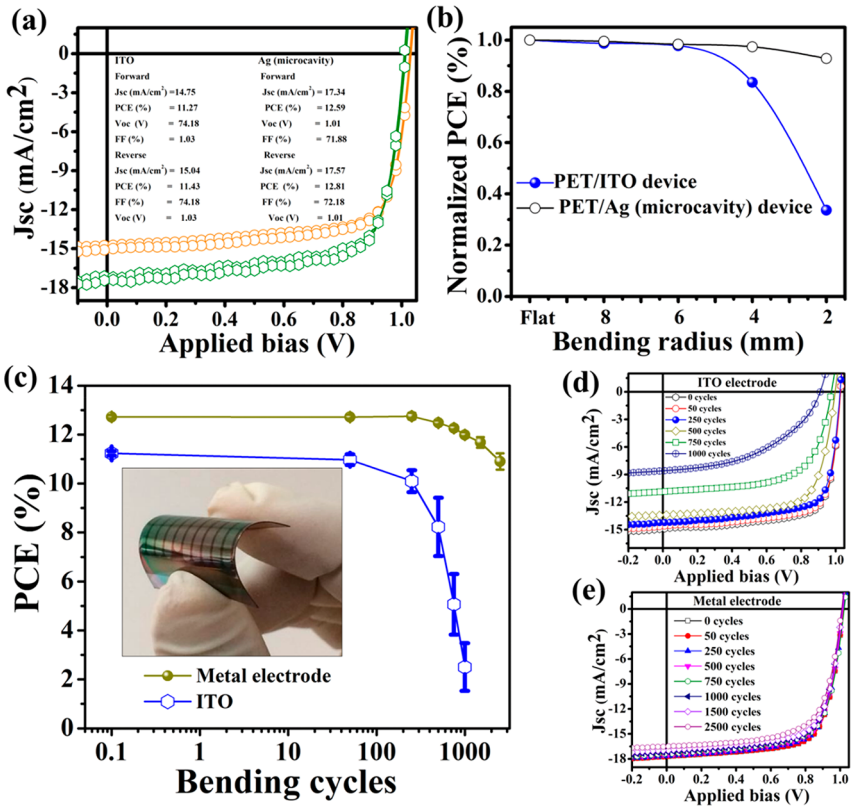


**Figure 9.** (a) $J-V$ curves of flexible PSC devices having metal and ITO electrodes. (b) Normalized PCEs of devices upon increasing the bending radius. (c) Normalized PCEs plotted with respect to the number of bending cycles at a fixed bending radius of 5 mm for the PET/Ag/$MoO_3$ and PET/ITO devices; average values from five separate devices are presented with error bars of standard deviation. Best $J-V$ curves upon varying the number of bending cycles for devices (d) ITO and (e) metal electrodes.

The average PL decay times ($\tau_{average}$) were calculated using the values of $\tau_i$ and $A_i$ from the fitted curve data in Table S3, using eq 2.[41]

$$\tau_{average} = \frac{\sum Ai\tau i^2}{\sum Ai\tau i} \quad (4)$$

The average PL decay time of Ag/PEDOT:PSS/perovskite was 8.44 ns. When ultrathin layers of $MoO_3$ (2, 4, 6 nm) were introduced between the Ag and PEDOT:PSS layers, the values of $\tau_{average}$ were all lower, at 4.79, 2.93, and 4.63 ns, respectively. A shorter PL decay time is beneficial for increasing the degree of quenching at the perovskite−HTL interface.[42,43]

**3.6. Photovoltaic Performances of PSCs with Various Cavity Electrodes.** Next, we examined whether our microcavity strategy could be applied using other metal electrodes (Au, Cu, Al, Ag) having microcavity structures and to ITO-based semitransparent PSCs. Figure 8a and Table S3 present the $J-V$ curves and photovoltaic parameters of the best performing of the various bottom electrode and semitransparent devices under air mass 1.5 global (AM 1.5G) 1-sun illumination at 100 mW/cm$^2$. Under front illumination, the semitransparent PSCs had lower values of $J_{sc}$ than those of the cavity (Au, Ag, Al, Cu) electrode-based devices, because no optical interference occurred at the ITO electrode. The PCEs of the Al-based devices were lower, and they exhibited some hysteresis, when compared with the various other metal electrodes, because the roughness of the Al electrode was high (Figure S9). The performance of the Cu-based device was, however, poor because the electrode's WF did not change after the doping of $MoO_3$.[38] The barrier between Cu and the HTL was very high, making it difficult to collect the holes from the HTL to the electrode; for this reason, the FF of this device was poor. As displayed in Figure 8b, the EQEs and integrated $J_{sc}$ of the semitransparent PSCs with ITO and the PSCs with cavity electrodes were comparable under front illumination at short wavelengths (350−500 nm), but the semitransparent devices had lower EQEs at longer wavelengths (500−800 nm) because there was no optical interference at the electrode. In the cavity electrode PSC devices, the thick metal electrode served as a rear reflector that increased the path length of light inside the active layer, thereby enhancing the harvesting of photons of longer wavelength. The values of $J_{sc}$ integrated from the EQE spectra were 16.82 and 14.28 mA/cm$^2$, respectively, closed to our experimentally determined values. Long-term stability is important in PSCs for commercial application; semitransparent PSCs with ITO electrodes generally display good PCE performance, but their stability is poor.[44−48] Figure 8c presents the results of stability tests of the cells having metal and ITO electrodes, measured in a $N_2$-filled glovebox. After 72 days of storage and testing, the PCE of the ITO/PEDOT:PSS cell degraded to 44% of its initial value, while that of the Au/$MoO_3$ (4 nm)/PEDOT:PSS cell degraded to 9% from its initial value. The decreases in device performance mainly arose from decreases in the FFs (inset in Figure 8c). The decrease in PCE of the semitransparent device occurred primarily because ITO reacted with the weakly acidic PEDOT:PSS;[49] in contrast, metal electrodes are very insensitive to such acids. Nevertheless, the PCEs of the Al-, Ag-, and Cu-based devices degraded to 84%, 95%, and 5%, respectively, from their initial PCEs (Figure


DOI: 10.1021/acsami.8b04329
ACS Appl. Mater. Interfaces XXXX, XXX, XXX−XXX

S10). The perovskite was much more stable in devices having Cu and Au metallic electrodes, but the Ag- and Al-based devices were unstable because of strong reactions occurring with the perovskite halides.[50]

## 4. PERFORMANCE OF FLEXIBLE PEROVSKITE SOLAR CELLS

Furthermore, employing the microcavity structure, we also fabricated flexible PSCs on PET substrates having same effective active area. Figure 9a presents the $J-V$ curves of the best-performing PET/Ag and PET/ITO devices, measured in both forward and reverse bias sweeps. The devices exhibited less hysteresis with respect to the scan direction, in good agreement with the $J-V$ behavior of previously reported flexible PSCs.[8,51] One of the greatest advantages of flexible substrates over rigid substrates is mechanical bending flexibility under bending stress. Figure 9b displays the relationship between the PCE and the bending radius (8, 6, 4, 2 mm) after one bending cycle for the PET/Ag and PET/ITO cells. The PCEs of the PET/Ag and PET/ITO devices decreased only slightly, even after bending with a radius of 8 mm; in contrast, they decreased to 97 and 83%, respectively, of their original values when the bending radius was 4 mm. These PCEs decreased further, to 92% and 33%, respectively, when the bending radius decreased again to 2 mm. Figure 9c displays the relationship between the average PCEs of three PET/Ag and PET/ITO devices and the number of bending cycles when bending radius was 5 mm. Although the PCEs of the PET/ITO devices decreased slightly to 96% of its initial value at the beginning of bending, it decreased rapidly when increasing the number of bending cycles to 250; the best values of PCE after 500, 750, and 1000 bending cycles (at 5 mm) all decreased to 83, 60, and 33%, respectively, of the initial value. In addition, the values of $J_{sc}$, $V_{oc}$, and FF gradually decreased upon increasing the number of bending cycles (Figure S11). The poorer photovoltaic parameters arose because the sheet resistance increased upon bending, due to the generation of cracks on the ITO.[10] In comparison, the performance of the PET/Ag device was more stable with respect to the number of bending cycles at 5 mm (Figure 9c), with only a 14.8% decrease from the initial value of PCE after 2500 bending cycles. Figure 9d,e display the evolution of the best $J-V$ curves of the PET/ITO and PET/Ag devices, respectively, throughout 1000 and 2500 bending cycles at 5 mm. For the PET/ITO device, the values of $J_{sc}$ and the FFs underwent to greatest decreases upon increasing the number of bending cycles; accordingly, the PCE decreased rapidly (Figure 9c). On the other hand, the best $J-V$ curves for the PET/Ag device remained almost consistent throughout the 2500 bending cycles (Figure 9c). As illustrated in Figure S12f, the perovskite film retained its cubic structure, with the same full width at half-maximum after 1500 or 2500 bending cycles, indicating that the crystallinity of the film did not change upon increasing the number of bending cycles. Meanwhile, the perovskite film surface morphology, determined through SEM at normal resolution, did not change in after 1500 or 2500 bending cycles (Figures S12a–c). High-resolution SEM images (Figures S12d,e), however, revealed some pinholes between the grain boundaries after 2500 bending cycles, and these features were responsible for the decrease in PCE.

## 5. CONCLUSIONS

We have used a combination of theoretical simulations and experimental investigations to investigate the properties of top-illuminated ITO-free PSCs having microcavity structures. We fabricated the devices incorporating microcavity structures through the insertion of ultrathin $MoO_3$ layers on top of the cavity electrode. Introducing the ultrathin $MoO_3$ layer on the anode surface resulted in the enhanced interface formation, excellent energy level alignment, and efficient charges carrier extraction between the metal and the HTL. At the optimized thickness of the ultrathin $MoO_3$ layer on the metal electrode, the best hysteresis-free PCE was 13.54%. From a study of the PSCs with different microcavity structure electrodes, we found that Au and Cu anodes based devices exhibited improved stability (up to 72 days) without losing device performance. Flexible devices having the microcavity structure exhibited excellent bending durability, retaining over 86% of its original PCE after 2500 full bending cycles. The results of this study suggest that such highly flexible devices could be effective power sources for portable and wearable electronics.

## ■ ASSOCIATED CONTENT

### Supporting Information

The Supporting Information is available free of charge on the ACS Publications website at DOI: 10.1021/acsami.8b04329.

Each layer extinction coefficient and refractive index in the solar cell devices; simulated $J_{sc}$ values of devices with respect to transport layer thicknesses versus active layer thicknesses, full spectrum of UPS various doped $MoO_3$ on cavity electrode, TRPL of glass/Ag/perovskite and SEM photogh of 330 nm perovskite layer thickness, average device (60) parameters (FF, $J_{sc}$, $V_{oc}$) of PSCs and stability of device various microcavity electrodes (Al, Ag, Cu), photovoltaics parameters of flexible devices with respect to ITO and metal electrodes, XRD and SEM of perovskite film bending stability with respect to 5 mm radius, and tables containing the device parameters, comparison with other reported papers, and TRPL parameters (PDF)

## ■ AUTHOR INFORMATION


### Corresponding Authors

*E-mail: hwlin@mx.nthu.edu.tw.
*E-mail: cslai@mail.cgu.edu.tw.
*E-mail: gchu@gate.sinica.edu.tw.

### ORCID

Karunakara Moorthy Boopathi: 0000-0003-2042-9595
Hao-Wu Lin: 0000-0003-4216-7995
Yia-Chung Chang: 0000-0003-1851-4651
Yun-Chorng Chang: 0000-0002-2862-9789
Chao-Sung Lai: 0000-0002-2069-7533
Chih-Wei Chu: 0000-0003-0979-1729


### Notes

The authors declare no competing financial interest.

## ■ ACKNOWLEDGMENTS

C.-W.C. thanks the Ministry of Science and Technology (MOST) of Taiwan (104-2221-E-001-014-MY3 and 104-2221-E-009-096-MY3) and the Career Development Award of Academia Sinica, Taiwan (103-CDA-M01), for financial support. C.-S.L., thanks MOST (106-2221-E-182-059-MY3,



DOI: 10.1021/acsami.8b04329
ACS Appl. Mater. Interfaces XXXX, XXX, XXX–XXX

106-2632-E-182-001, and 106-2911-I-182-504) and Chang Gung Memorial Hospital (CMRPD2F0022 and CMRPD2G0101) for financial support.

## REFERENCES

(1) Green, M. A.; Ho-Baillie, V.; Snaith, H. J. The Emergence of Perovskite Solar Cells. *Nat. Photonics* **2014**, *8*, 506.
(2) Jung, H. S.; Park, N.-G. Perovskite Solar Cells: From Materials to Devices. *Small* **2015**, *11*, 10.
(3) Kim, H. S.; Lee, C. R.; Im, J. H.; Lee, K. B.; Moehl, T.; Marchioro, A.; Moon, S. J.; Humphry-Baker, R.; Yum, J. H.; Moser, J. E.; Gratzel, M.; Park, N. G. Lead Iodide Perovskite Sensitized All-Solid-State Submicron Thin Film Mesoscopic Solar Cell with Efficiency Exceeding 9%. *Sci. Rep.* **2012**, *2*, 591.
(4) Xing, G. C.; Mathews, N.; Sun, S. Y.; Lim, S. S.; Lam, Y. M.; Gratzel, M.; Mhaisalkar, S.; Sum, T. C. Long-Range Balanced Electronand Hole-Transport Lengths in Organic-Inorganic $CH_3NH_3PbI_3$. *Science* **2013**, *342*, 344.
(5) Stranks, S. D.; Eperon, G. E.; Grancini, G.; Menelaou, C.; Alcocer, M. J. P.; Leijtens, T.; Herz, L. M.; Petrozza, A.; Snaith, H. J. Electron-Hole Diffusion Lengths Exceeding 1 Micrometer in an Organometal Trihalide Perovskite Absorber. *Science* **2013**, *342*, 341.
(6) Yang, W. S.; Park, B. W.; Jung, E. H.; Jeon, N. J.; Kim, Y. C.; Lee, D. U.; Shin, S. S.; Seo, J.; Kim, E. K.; Noh, J. H.; Seok, S. I. Iodide Management in Formamidinium-Lead-Halide−based Perovskite Layers for Efficient Solar Cells. *Science* **2017**, *356*, 1376−379.
(7) Docampo, P.; Ball, J. M.; Darwich, M.; Eperon, G. E.; Snaith, H. J. Efficient Organometal Trihalide Perovskite Planar-Heterojunction Solar Cells on Flexible Polymer Substrates. *Nat. Commun.* **2013**, *4*, 2761.
(8) Li, Y.; Meng, L.; Yang, Y.; Xu, G.; Hong, Z.; Chen, Q.; You, J.; Li, G.; Yang, Y.; Li, Y. High-Efficiency Robust Perovskite Solar Cells on Ultrathin Flexible Substrates. *Nat. Commun.* **2016**, *7*, 10214.
(9) Chiang, C. H.; Nazeeruddin, M. K.; Gratzel, M.; Wu, C. G. The Synergistic Effect of $H_2O$ and DMF Towards Stable and 20% Efficiency Inverted Perovskite Solar Cells. *Energy Environ. Sci.* **2017**, *10*, 808−817.
(10) Kim, B. J.; Kim, D. H.; Lee, Y. Y.; Shin, H. W.; Han, G. S.; Hong, J. S.; Mahmood, K.; Ahn, T. K.; Joo, Y. C.; Hong, K. S.; Park, N. G.; Lee, S.; Jung, H. S. Highly Efficient and Bending Durable Perovskite Solar Cells: Toward a Wearable Power Source. *Energy Environ. Sci.* **2015**, *8*, 916.
(11) Yoon, J.; Sung, H.; Lee, G.; Cho, W.; Ahn, N.; Jung, H. S.; Choi, M. Superflexible, High-Efficiency Perovskite Solar Cells Utilizing Graphene Electrodes: Towards Future Foldable Power sources. *Energy Environ. Sci.* **2017**, *10*, 337−345.
(12) Park, N. G.; Gratzel, M.; Miyasaka, T.; Zhu, K.; Emery, K. Towards Stable and Commercially Available Perovskite Solar Cells. *Nat. Energy* **2016**, *1*, 16152.
(13) Acik, M.; Darling, S. B. Graphene in Perovskite Solar Cells: Device Design, Characterization and Implementation. *J. Mater. Chem. A* **2016**, *4*, 6185−6235.
(14) Habisreutinger, S. N.; Nicholas, R. J.; Snaith, H. J. Carbon Nanotubes in Perovskite Solar Cells. *Adv. Energy Mater.* **2017**, *7*, 1601839.
(15) Qin, F.; Tong, J.; Ge, R.; Luo, B.; Jiang, F.; Liu, T.; Jiang, Y.; Xu, Z.; Mao, L.; Meng, W.; Xiong, S.; Li, Z.; Li, L.; Zhou, I. Indium tin oxide (ITO)-Free, Top-illuminated, Flexible Perovskite Solar Cells. *J. Mater. Chem. A* **2016**, *4*, 14017−14024.
(16) Hsu, C. L.; Lin, C. T.; Huang, J. H.; Chu, C. W.; Wei, K. H.; Li, L. J. Layer-by-Layer Graphene/TCNQ Stacked Films as Conducting Anodes for Organic Solar Cells. *ACS Nano* **2012**, *6*, 5031−5039.
(17) Wang, X.; Li, Z.; Xu, W.; Kulkarni, S. A.; Batabyal, S. K.; Zhang, S.; Cao, A.; Wong, L. H. H.$TiO_2$ nanotube arrays based flexible perovskite solar cells with transparent carbon nanotube electrode. *Nano Energy* **2015**, *11*, 728−735.
(18) Huang, J. H.; Fang, J. H.; Liu, C. C.; Chu, C. W. Effective Work Function Modulation of Graphene/Carbon Nanotube Composite Films As Transparent Cathodes for Organic Optoelectronics. *ACS Nano* **2011**, *5*, 6262−6271.
(19) Aitola, K.; Sveinbjornsson, K.; Correa-Baena, J. P.; Kaskela, A.; Abate, A.; Tian, Y.; Johansson, E. M. J.; Gratzel, M.; Kauppinen, E. I.; Hagfeldt, A.; Boschloo, G. Carbon Nanotube-based Hybrid Hole-Transporting Material and Selective Contact for High Efficiency Perovskite Solar Cells. *Energy Environ. Sci.* **2016**, *9*, 461.
(20) Liu, Z.; You, P.; Xie, C.; Tang, G.; Yan, F. Ultrathin and Flexible Perovskite Solar Cells with Graphene Transparent Electrodes. *Nano Energy* **2016**, *28*, 151−157.
(21) Lin, H. W.; Chiu, S. W.; Lin, L. Y.; Hung, Z. Y.; Chen, Y. H.; Lin, F.; Wong, K. T. Device Engineering for Highly Effi cient Top-Illuminated Organic Solar Cells with Microcavity Structures. *Adv. Mater.* **2012**, *24*, 2269−2272.
(22) You, J.; Li, X.; Xie, F.; Sha, W. E. I.; Kwong, J. H. W.; Li, G.; Choy, W. C.H.; Yang, Y. Surface Plasmon and Scattering-Enhanced Low-Bandgap Polymer Solar Cell by a Metal Grating Back Electrode. *Adv. Energy Mater.* **2012**, *2*, 1203−1207.
(23) Zuo, L.; Chueh, C. C.; Xu, Y. X.; Chen, K.; Zang, Y.; Li, C. Z.; Chen, H.; Jen, A. K.Y. Microcavity-Enhanced Light-Trapping for Highly Effi cient Organic Parallel Tandem Solar Cells. *Adv. Mater.* **2014**, *26*, 6778.
(24) Lee, M.; Jo, Y.; Kim, D. S.; Jun, Y. Flexible Organo-Metal Halide Perovskite Solar Cells on a Ti Metal Substrate. *J. Mater. Chem. A* **2015**, *3*, 4129−4133.
(25) Troughton, J.; Bryant, D.; Wojciechowski, K.; Carnie, M. J.; Snaith, H. J.; Worsley, D. A.; Watson, T. M. Highly Efficient, Flexible, Indium-Free Perovskite Solar Cells Employing Metallic Substrates. *J. Mater. Chem. A* **2015**, *3*, 9141−9145.
(26) Lee, M.; Ko, Y.; Min, B. K.; Jun, Y. Silver Nanowire Top Electrodes in Flexible Perovskite Solar Cells using Titanium Metal as Substrate. *ChemSusChem* **2016**, *9*, 31−35.
(27) Boopathi, K. M.; Mohan, R.; Huang, T. Y.; Budiawan, W.; Lin, M. Y.; Lee, C. H.; Ho, K. C.; Chu, C. W. Synergistic Improvements in Stability and Performance of Lead Iodide Perovskite Solar Cells Incorporating Salt Additives. *J. Mater. Chem. A* **2016**, *4*, 1591−1597.
(28) Vitos, L.; Ruban, A. V.; Skriver, H. L.; Kollar, J. The surface energy of metals. *Surf. Sci.* **1998**, *411*, 186−202.
(29) Bi, C.; Wang, Q.; Shao, Y.; Yuan, Y.; Xiao, Z.; Huang, J. Non-Wetting Surface-Driven High-Aspect-Ratio Crystalline Grain Growth for Efficient Hybrid Perovskite Solar Cells. *Nat. Commun.* **2015**, *6*, 7747.
(30) Xiao, Z.; Bi, C.; Shao, Y.; Dong, Q.; Wang, Q.; Yuan, Y.; Wang, C.; Gao, Y.; Huang, J. Efficient, High Yield Perovskite Photovoltaic Devices Grown by Interdiffusion of Solution-Processed Precursor Stacking Layers. *Energy Environ. Sci.* **2014**, *7*, 2619−2623.
(31) Burkhard, G. F.; Hoke, E. T.; McGehee, M. D. Accounting for Interference, Scattering, and Electrode Absorption to Make Accurate Internal Quantum Efficiency Measurements in Organic and Other Thin Solar Cells. *Adv. Mater.* **2010**, *22*, 3293−3297.
(32) Armin, A.; Velusamy, M.; Wolfer, P.; Zhang, Y.; Burn, P. L.; Meredith, P.; Pivrikas, A. Quantum Efficiency of Organic Solar Cells: Electro-Optical Cavity Considerations. *ACS Photonics* **2014**, *1*, 173−181.
(33) Kim, H. S.; Park, N. G. Parameters Affecting I−V Hysteresis of CH3NH3PbI3 Perovskite Solar Cells: Effects of Perovskite Crystal Size and Mesoporous TiO2 Layer. *J. Phys. Chem. Lett.* **2014**, *5*, 2927−2934.
(34) Sanchez, R. S.; Gonzalez-Pedro, V.; Lee, J. W.; Park, N. G.; Kang, Y. S.; Mora-Sero, I.; Bisquert, J. Slow Dynamic Processes in Lead Halide Perovskite Solar Cells. Characteristic Times and Hysteresis. *J. Phys. Chem. Lett.* **2014**, *5*, 2357−2363.
(35) Snaith, H. J.; Abate, A.; Ball, J. M.; Eperon, G. E.; Leijtens, T.; Noel, N. K.; Stranks, S. D.; Wang, J. T.W.; Wojciechowski, K.; Zhang, W. Slow Dynamic Processes in Lead Halide Perovskite Solar Cells. Characteristic Times and Hysteresis. *J. Phys. Chem. Lett.* **2014**, *5*, 1511−1515.


DOI: 10.1021/acsami.8b04329
*ACS Appl. Mater. Interfaces* XXXX, XXX, XXX−XXX

(36) Kim, H. S.; Jang, I. H.; Ahn, N.; Choi, M.; Guerrero, A.; Bisquert, J.; Park, N. G. Control of I–V Hysteresis in $CH_3NH_3PbI_3$ Perovskite Solar Cell. *J. Phys. Chem. Lett.* **2015**, *6*, 4633–4639.
(37) Qin, P.; Fang, G.; Ke, W.; Cheng, F.; Zheng, Q.; Wan, J.; Lei, H.; Zhao, X. In Situ Growth of Double-Layer $MoO_3/MoS_2$ Film from $MoS_2$ for Hole-Transport Layers in Organic Solar Cell. *J. Mater. Chem. A* **2014**, *2*, 2742.
(38) Greiner, M. T.; Chai, L.; Helander, M. G.; Tang, W. M.; Lu, Z. H. Metal/Metal-Oxide Interfaces: How Metal Contacts Affect the Work Function and Band Structure of $MoO_3$. *Adv. Funct. Mater.* **2013**, *23*, 215.
(39) Liu, Z.; Kobayashi, M.; Paul, B. C.; Bao, Z.; Nishi, Y. Contact Engineering for Organic Semiconductor Devices via Fermi Level Depinning at the Metal-Organic Interface. *Phys. Rev. B: Condens. Matter Mater. Phys.* **2010**, *82*, 035311.
(40) Kang, N.; Hoang, M.; Choi, D.; Ju, B. K.; Hong, J. M.; Yu, J. W. Enhanced Performance of Organic Photovoltaic Devices by Photo-Crosslinkable Buffer Layer. *Macromol. Res.* **2013**, *21*, 65.
(41) Wu, B.; Fu, Z. K.; Yantara, N.; Xing, G.; Sun, S.; Sum, T. C.; Mathews, N. Charge Accumulation and Hysteresis in Perovskite-Based Solar Cells: An Electro-Optical Analysis. *Adv. Energy Mater.* **2015**, *5*, 1500829.
(42) Zhu, Z.; Ma, J.; Wang, Z.; Mu, C.; Fan, Z.; Du, L.; Bai, Y.; Fan, L.; Yan, H.; Phillips, S.; Yang, D. L. Efficiency Enhancement of Perovskite Solar Cells through Fast Electron Extraction: The Role of Graphene Quantum Dots. *J. Am. Chem. Soc.* **2014**, *136*, 3760.
(43) Liang, P. W.; Liao, C. Y.; Chueh, C. C.; Zuo, F.; Williams, S. T.; Xin, X. K.; Lin, J.; Jen, A. K. Y. Additive Enhanced Crystallization of Solution-Processed Perovskite for Highly Efficient Planar-Heterojunction Solar Cells. *Adv. Mater.* **2014**, *26*, 3748–3754.
(44) National Renewable Energy Laboratory. Best Research Cell Efficiency. http://www.nrel.gov/ncpv/images/efficiency_chart.jpg.
(45) Service, R. F. Perovskite Solar Cells Keep On Surging. *Science* **2014**, *344*, 458.
(46) Park, N. G. Organometal Perovskite Light Absorbers Toward a 20% Efficiency Low-Cost Solid-State Mesoscopic Solar Cell. *J. Phys. Chem. Lett.* **2013**, *4*, 2423–2429.
(47) McGehee, M. D. Fast-track solar cells. *Nature* **2013**, *501*, 323–325.
(48) Zhou, H.; Chen, Q.; Li, G.; Luo, S.; Song, T.; Duan, S. H.; Hong, Z.; You, J.; Liu, Y.; Yang, Y. Interface Engineering of Highly Efficient Perovskite Solar Cells. *Science* **2014**, *345*, 542–546.
(49) Liu, Z.; He, T.; Wang, H.; Song, X.; Liu, H.; Yang, J.; Liu, K.; Ma, H. Improving the Stability of The Perovskite Solar Cells by V2O5Modified Transport Layer Film. *RSC Adv.* **2017**, *7*, 18456–18465.
(50) Deng, Y.; Dong, Q.; Bi, C.; Yuan, Y.; Huang, J. Air-Stable, Effi cient Mixed-Cation Perovskite Solar Cells with Cu Electrode by Scalable Fabrication of Active Layer. *Adv. Energy Mater.* **2016**, *6*, 1600372.
(51) Bi, C.; Chen, B.; Wei, H.; DeLuca, S.; Huang, J. Efficient Flexible Solar Cell based on Composition-Tailored Hybrid Perovskite. *Adv. Mater.* **2017**, *29*, 1605900.


DOI: 10.1021/acsami.8b04329
*ACS Appl. Mater. Interfaces* XXXX, XXX, XXX–XXX